

# “Fluid bearing” effect of enclosed liquids in grooves on drag reduction in microchannels

Haosheng Chen and Yang Gao

*State Key Laboratory of Tribology, Tsinghua University, Beijing 100084, China*

Howard A. Stone

*Department of Mechanical and Aerospace Engineering, Princeton University,  
Princeton, New Jersey 08544, USA*

Jiang Li\*

*School of Mechanical Engineering, University of Science and Technology Beijing, Beijing 100083, China*

(Received 19 May 2016; published 28 December 2016)

We report details of the fluid motion formed within and above grooves when a laminar continuous phase fluid flows over a second immiscible fluid enclosed in a grooved microchannel. Vortical structures within the transverse grooves were caused by a slip velocity at the fluid-fluid interface and act as “fluid bearings” on the boundary to lubricate the flow of the continuous phase. We investigated the drag reduction in the laminar flow in the microchannel by measuring slip at the boundaries and calculating an effective slip length, taking into account the influence of the effect of the viscosity ratio of the two fluids on the effective slip length. The “fluid bearing” effect can be used to transport high viscosity fluids using low viscosity fluids trapped in cavities to reduce drag.

DOI: [10.1103/PhysRevFluids.1.083904](https://doi.org/10.1103/PhysRevFluids.1.083904)

## I. INTRODUCTION

Fluid motion is significantly affected by the properties of the adjacent solid surfaces, such as roughness and wetting conditions [1]. With the development of micro- and nanofluidic devices and networks, the increasing large surface-to-volume ratio increases the relative influence of friction on the flow [2,3]. A rough surface is known to increase drag in turbulent channel flows and the larger fluid-solid contact area might be expected to slow down the flow for the laminar low Reynolds number flows characteristic of microfluidic configurations. However, for fluid flows over rough superhydrophobic surfaces with trapped air, the drag force can be reduced by an effective slip boundary of the liquid-air interface [4–9]. The liquid-air interface can be substituted by a liquid-liquid interface in applications of porous media filled with another liquid [10–12] or the lubricant-impregnated surfaces [13,14], and drag reduction was observed in experiments with rheometers in both the laminar flow regime [14] and the turbulent flow regime [15]. As microfluidic systems in a variety of applications may utilize high viscosity fluids, such as viscous oils, sols, and solutions containing nanoparticles, proteins, or polymers, drag reduction enabled by a fluid-fluid interface can have potential applications for laminar flows of high viscosity fluids, which is always a challenge that arises with miniaturization and in tribological applications.

Flows in microchannels are typically laminar [16]. When a fluid is enclosed in the grooves of a microchannel by another immiscible fluid, the surface is in the Cassie state, and a (periodic) no-slip/slip boundary condition is formed. One approach to model such a heterogeneous no-slip/slip boundary is to introduce an effective slip length. The effect of slip length on the drag reduction has been theoretically analyzed for the case of perfect slip [16]. Recently, more detailed calculations

---

\*lijiang@ustb.edu.cn

have been given for the case of cavities filled with a viscous fluid, and both the theoretical and the numerical results exhibit a significant effect of the viscosity ratio of the two fluids on the slip velocity [17,18]. However, there are no corresponding experimental results yet to evaluate the slip boundary and laminar channel flow with realistic shapes of the fluid-fluid interface, including how the viscosity ratios of the two fluids influence the slip velocities at the boundary. We report the results of such experiments, which allow assessment of the idealized mathematical models.

In this work, we constructed microfluidic devices that allow a continuous phase fluid to flow over transverse-oriented cavities filled with another immiscible fluid to form a Cassie state in the microchannel. The flow of the continuous phase acts on the fluid-fluid interface, and drives a vortical flow of the enclosed fluid within the cavities, which act as “fluid bearings” to reduce the drag on the continuous phase. We study the influence of the viscosity ratio of the two fluids on the “fluid bearing” effect for water-on-oil, oil-on-water, and water-on-air flows. Microparticle image velocimetry ( $\mu$ PIV) was used to measure the vortical flow fields within the cavities and the velocity field along the heterogeneous substrate, which allows an estimate of an effective slip length to be compared with the effective slip length derived from a direct measurement of the pressure drop as a function of the flow rate. Although the drainage of the enclosed fluid may cause the failure of the no-slip/slip boundary [19], the fluid stays trapped in the cavities for all of the conditions we study.

## II. EXPERIMENTAL APPROACH

A polydimethylsiloxane (PDMS) microfluidic device was made using soft lithography methods. The device consisted of two main parallel microchannels: the primary channel for the continuous phase to be transported and the secondary channel for the enclosed fluid that imparts a slip boundary condition. The two main channels were connected by an array of side channels, which have wider openings located along one side of the primary channel, as shown in Figs. 1(a) and 1(b). Two immiscible fluids were driven into the main parallel channels individually by two separate channels of a pressure controller (MFCS<sup>TM</sup>, Fluigent Inc.), which had a pressure output range of 0–1000 mbar with a resolution of 1 mbar. The enclosed fluid was injected into the secondary channel and filled the array of side channels and the grooves first. Then the continuous phase was injected into the other main channel to form a continuous flow over the enclosed fluid in the grooves, which resulted in periodic fluid-fluid interfaces over the grooves along one side of the primary channel, as shown in Figs. 1(b) and 1(c). The width of the main channel for the continuous phase is 400  $\mu\text{m}$ , and the total length of the grooved section is 4.5 mm, where the periodic length of the grooves is 300  $\mu\text{m}$  with the width  $b = 200 \mu\text{m}$  and the depth  $h = 100 \mu\text{m}$  of the cavity, respectively. The height of the channel is 25  $\mu\text{m}$ . The shape of the fluid-fluid interfaces were kept approximately flat during the experiments by adjusting the pressure applied on the enclosed fluid. As the difference between the protrusion angles at different grooves along the same channel can be controlled to less than  $10^\circ$ , here we neglect the effect of the shapes of the interfaces [20].

The two immiscible fluids were paraffin oil and an aqueous solution of different concentrations of glycerol. The viscosity of the paraffin oil is 29.5 mPa s, while the viscosities of the glycerol solutions were 1.00, 2.13, 6.01, and 35.5 mPa s for concentrations of 0, 25, 50, and 75 wt% glycerol, respectively. Interchanging the oil and the glycerol solutions enables us to vary the viscosity ratio  $N = \eta_c/\eta_e$  from 0.03 to 29.5, where  $\eta_c$  and  $\eta_e$  are the viscosities of the continuous phase and the enclosed fluid, respectively. The interfacial tension  $\sigma$  between the different combinations of the paraffin oil and the glycerol solutions is in the range of 19.9–27.7 mN/m. Consequently, in the experiments, the capillary numbers are  $\text{Ca} = \eta_c u/\sigma = O(10^{-2})$  and the Reynolds numbers are  $\text{Re} = \rho_c u d_H/\eta_c < 0.1$ , where  $u$  and  $\rho_c$  are the average velocity and the density of the continuous phase, respectively,  $d_H = 4C/P$  is the hydraulic diameter, and  $C$  and  $P$  are the area and perimeter of the channel cross section, respectively [8,9]. Therefore, all the flows involved in our experiments are laminar flows.

To prevent the grooves from wetting by the continuous phase, the groove surfaces were chemically treated to be nonwetting for the continuous phase. For example, when the enclosed fluid is oil, the

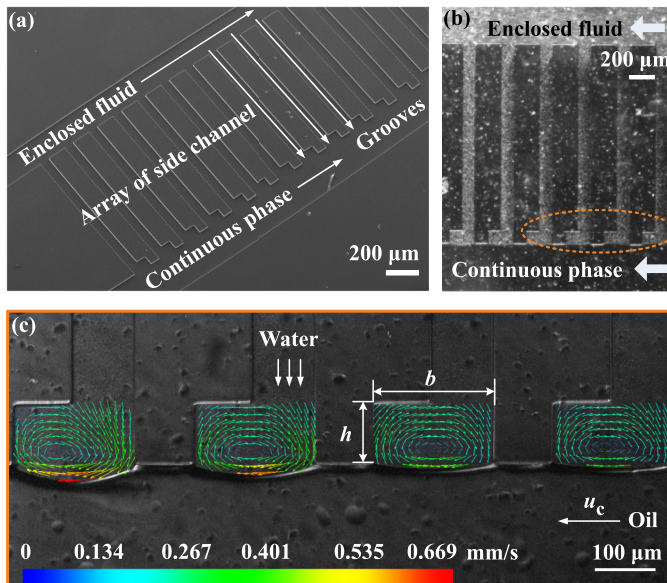


FIG. 1. The design of the PDMS device and the typical flow field. (a) SEM image of the detailed design. Two main parallel channels were connected with an array of side channels, with wider grooves fabricated on one side of the main channel for the continuous phase. The detailed dimensions of the grooved channel are shown in Fig. 5(a) and Appendix A. (b) The grooves were filled with the enclosed fluid, which was seeded with fluorescent particles for  $\mu$ PIV measurements. (c) The velocity distributions of the enclosed fluid in the grooves obtained by  $\mu$ PIV. The flow of the enclosed fluid forms vortical structures in the grooves.

groove surfaces were treated to be hydrophobic by flowing octadecyltrichlorosilane (OTS) into the grooves prior to the experiments. Otherwise, the grooves were filled with water to maintain a hydrophilic condition soon after the bonding of the plasma-treated PDMS channel and the glass slide.

The aqueous solution was seeded with 1- $\mu$ m-diameter fluorescent particles and the velocity distributions were measured using  $\mu$ PIV. Image pairs with a delay time of 7  $\mu$ s between two exposures were acquired from  $\mu$ PIV, and 150 image pairs were averaged in time to obtain velocity profiles with a spatial resolution of 5.2  $\mu$ m  $\times$  2.6  $\mu$ m. For example, when aqueous solution was used as the enclosed fluid, stable vortices were observed in the grooves, as shown in Fig. 1(c); the trapped fluid acts as “fluid bearings” embedded in the grooves, and the slip velocities at the fluid-fluid interfaces can be measured.

In addition, the average flow rate of the continuous phase was monitored by a flow flux sensor (Fluigent Inc.) with a resolution of 0.5  $\mu$ L/min. A straight channel with the same dimensions as the primary channel, which had no grooves on the side wall, was made as a reference in the same device. The average flow rate of the continuous phase in the grooved channel is defined as  $Q_g$ , while the average flow rate of the continuous phase in the simple straight channel with no grooves is defined as  $Q_0$ .

### III. EXPERIMENTAL RESULTS

We first investigated the slip velocity at the fluid-fluid interface and the effect of the viscosity ratio  $N$ . The motion of the fluid-fluid interface created a vortical structure, and so acted as a slip boundary for the continuous phase flow, as shown in Fig. 2(a). Also, we report the results for  $N = \eta_c/\eta_e = 13.8, 4.9, 0.83$  with a fixed driving pressure 400 mbar of the continuous phase, where

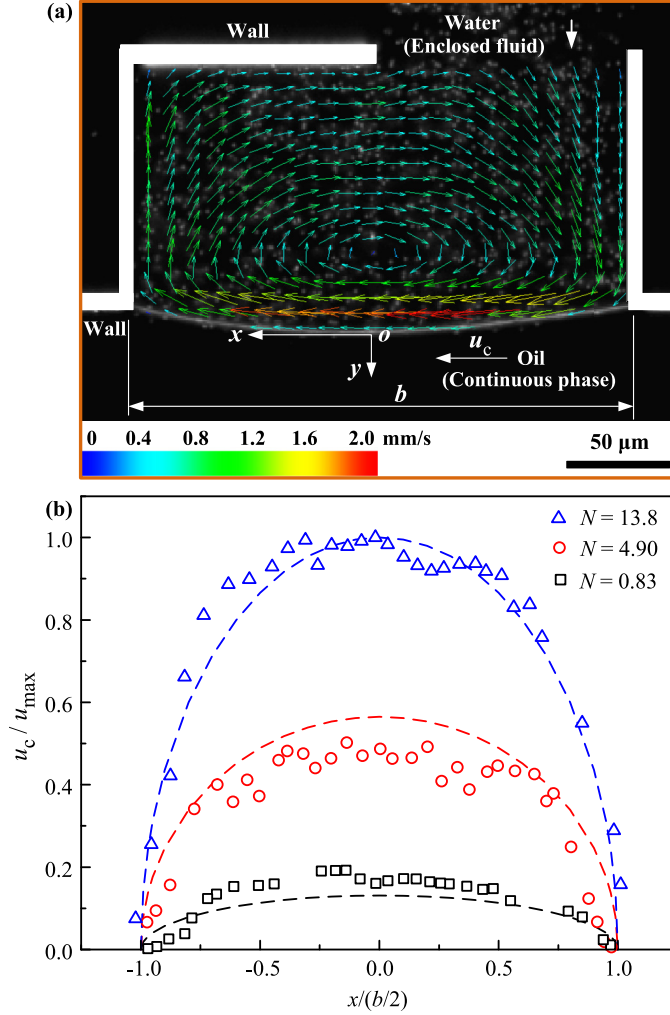


FIG. 2. The velocity distribution of the enclosed fluid in the grooves. (a) The velocity distribution of a single vortex in a groove for  $N = 13.8$ . The driving pressure of the oil is 400 mbar. (b) The normalized velocities  $u_c/u_{\max}$  at the fluid-fluid interface for  $N = 0.83, 4.9,$  and  $13.8$ , respectively, where  $u_{\max}$  is the maximum velocity at  $x = 0$  for  $N_{\text{ref}} = 13.8$ . The dashed lines are the theoretical results derived according to Eq. (1) with  $D = 0.027$ .

the continuous phase was paraffin oil and the enclosed fluids were 25, 50, 70 wt% glycerol solutions, respectively, as shown in Fig. 2(b), where  $x$  denotes the flow direction and  $b$  is the width of the groove. We measured the  $x$  component of the velocity distribution  $u_c(x)$  of the enclosed water phase at the interface, and observed that  $u_c(x)$  had an elliptic profile with a maximum velocity  $u_c(0)$  at  $x = 0$ . As the viscosity ratio  $N$  decreased, which corresponded to an increase of  $\eta_e$ , the value of  $u_c(0)$  decreased accordingly. Therefore, the highest velocity  $u_{\max}$  in the experiments is  $u_c(0)$  at the interface between oil and the aqueous solution with  $N_{\text{ref}} = 13.8$ , and the velocities  $u_c$  in Fig. 2(b) have been normalized with  $u_c/u_{\max}$ .

The flow along a heterogeneous substrate with periodic fluid-fluid interfaces can be interpreted as a Navier slip condition. Detailed fluid dynamical models assume the interface is flat and treat the flow in each cavity using the continuity of velocity and shear stress, i.e.,  $u_c = u_e$  and  $\eta_c \partial u_c / \partial y = \eta_e \partial u_e / \partial y$ ,

where the subscripts  $c$  and  $e$  represent the continuous and enclosed fluids respectively, and  $y$  is normal to the boundary. For  $|x| \leq b/2$  and  $y = 0$ , an effective slip boundary condition at the boundary [17] is expressed as  $u_c = N\gamma(x)\partial u_c/\partial y$ , where  $\gamma(x) = 2D[(b/2)^2 - x^2]^{1/2}$  is the local slip length distribution caused by the flow of the enclosed fluid in the grooves and  $D = \gamma(0)/b$  is the normalized maximum slip length, which depends on the shape of the grooves and the center of the vortices in the low-Reynolds-number flow [21]. Consequently, the normalized velocity  $u_c/u_{\max}$  can then be obtained as

$$\frac{u_c}{u_{\max}} = \frac{N}{N_{\text{ref}}} \left( \frac{1 + 4DN}{1 + 4DN_{\text{ref}}} \right) \sqrt{1 - \left( \frac{x}{b/2} \right)^2}, \quad (1)$$

where we have given details in Appendix B. Here, the slip is considered to be caused mainly by the hydrodynamics of the fluid inside the grooves while molecular slip is negligible. According to Eq. (1), the slip velocity for the continuous phase flow has an elliptic profile and is approximately proportional to the viscosity ratio  $N$ . The theoretical results of the normalized slip velocity,  $u_c/u_{\max}$ , are represented by the dashed lines in Fig. 2(b), and they show good agreement with the experiment results, taking into account the influence of the viscosity ratios. Therefore, the fluid-fluid interfaces change the no-slip boundary of the solid surface to a periodic no-slip/slip boundary, hence a slip velocity can be designed by the grooves shape and the viscosity ratios of the two fluids.

We then investigated the effective slip length of the “fluid bearing.” The fluid-fluid interfaces distributed along the channel wall form a periodic fluid-to-solid boundary for the flow of the continuous phase, as presented in Fig. 3(a). In Fig. 3(a), the width of the main channel for the continuous phase is  $100 \mu\text{m}$ , and the total length of the grooved section is  $6 \text{ mm}$ , where the periodic length of the grooves is  $300 \mu\text{m}$  with the width  $b = 100 \mu\text{m}$  and the depth  $h = 50 \mu\text{m}$  of the cavity, respectively. The height of the channel is  $25 \mu\text{m}$ . The increased velocity at the fluid-fluid interface will raise the average velocity along the entire boundary, and results in an effective slip length. Here we compared two different methods to estimate the effective slip length of the heterogeneous channel: One is to measure the velocity gradient with the  $\mu\text{PIV}$  method; the other is to directly measure the pressure-induced variation of the flow rate.

For the  $\mu\text{PIV}$  method, the effective slip length  $b_{\text{eff}}$  is calculated based on the average velocity profiles  $u_x|_{y=0} = b_{\text{eff}}(du_x/dy)|_{y=0}$  [20]. To acquire the velocity gradient  $du_x/dy$  of the continuous phase, the velocity variation along the  $y$  axis,  $u_x(y)$ , was measured using the  $\mu\text{PIV}$  method, as shown in Figs. 3(b) and 3(c), where the continuous phase was a glycerol solution and the enclosed fluid was paraffin oil. The measured velocity at the same  $y$  position was averaged both in time and in space, and a least-square linear fitting was performed for these averaged data below  $y = 15 \mu\text{m}$ . Thus, from the finite velocity extrapolated at  $y = 0$ , we obtain  $b_{\text{eff}}$  from the fitted lines in Fig. 3(d). The effective slip length  $b_{\text{eff}}$  was found to increase with the increase of the viscosity ratio  $N$ ; the continuous phase with higher viscosity has a smaller velocity gradient  $du_x/dy$  approaching the boundary, which results in a larger effective slip length.

For the direct measurement method, the effective slip length [15]  $\lambda_{\text{eff}}$  for a channel with a rectangular cross section of width  $W$  and height  $H$  [8,9] is evaluated according to the measured flow rate

$$\lambda_{\text{eff}} = \left( \frac{Q_g}{Q_o} - 1 \right) \frac{H}{3}, \quad (2)$$

where we have given details in the Appendix C. According to the measured flow rate under different driving pressures in Fig. 4(a), we evaluated  $\lambda_{\text{eff}}$  with Eq. (2) as shown in Fig. 4(b), where  $\lambda_{\text{eff}}$  is independent of the driving pressure, but depends on the viscosity ratio  $N$ .

We compared the effective slip length obtained from the two methods,  $b_{\text{eff}}$  and  $\lambda_{\text{eff}}$ , in Fig. 4(c), and found the best fit line has a slope about 0.9, which indicates the two methods give similar results; the bias of the fitted line indicates that the  $\mu\text{PIV}$  method underestimated the effective slip length. In addition, the larger effective slip lengths characteristic of higher viscosity ratios indicate, not

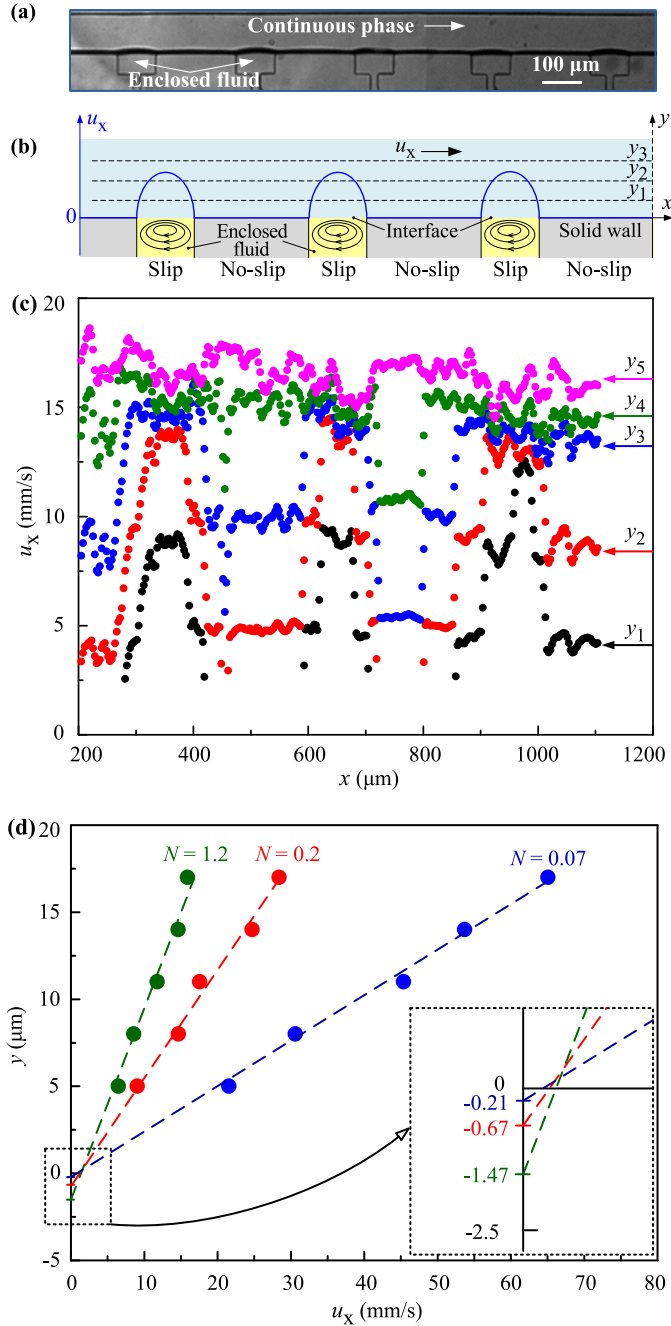


FIG. 3. The slip length measured in a grooved channel. (a) The periodic fluid-fluid interfaces under a driving pressure for the continuous phase of 400 mbar. The detailed dimensions of the grooved channel are shown in Fig. 5(b) and Appendix A. (b) The  $x$  component of velocity,  $u_x$ , on the grooved surface. The fluid-fluid interface and the solid surface form a periodic no-slip/slip boundary for the continuous phase. (c) The measured  $x$  component of velocities of the continuous phase ( $N = 1.2$ ) at different  $y$  positions, where  $y_1$ – $y_5$  are 5, 8, 11, 14, 17  $\mu\text{m}$ , respectively. (d) The measured average velocity distribution near the channel wall, where the dashed lines represent the linear fits for the effective slip length of the continuous phase with different viscosities.

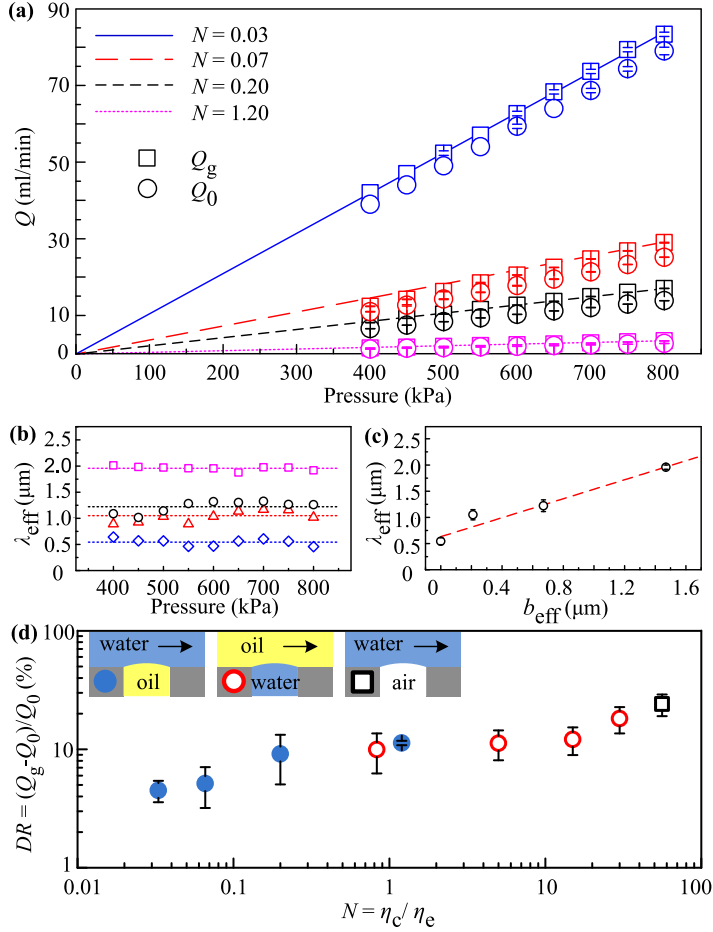


FIG. 4. Effective slip length and drag reduction of the fluid bearing effect. (a) The measured flow rates of the continuous phase fluids under different driving pressures in the water-on-oil system. The lines are the linear fitted results of  $Q_g$ . (b) Effective slip length  $\lambda_{\text{eff}}$  obtained from the direct measurement method with  $N = 1.2$  (squares), 0.2 (circles), 0.07 (triangles), and 0.03 (diamonds). The dotted lines indicate the average values. (c) Comparison of the effective slip lengths  $b_{\text{eff}}$  and  $\lambda_{\text{eff}}$  evaluated with the  $\mu\text{PIV}$  method and the direct measurement method. The experimental values and error bars of  $\lambda_{\text{eff}}$  (circle symbols) are obtained from the experimental results in (b). The dashed line is the linear fit line with a slope of 0.9. (d) The effect of the viscosity ratio  $N$  on the drag reduction. The driving pressure of the continuous phase for all the experimental data was 400 mbar except for the water-on-air flow, for which the driving pressure was 200 mbar.

surprisingly, that a more viscous fluid can be transported more efficiently with less drag force by flowing over an immiscible fluid with lower viscosity enclosed in grooves.

Next, we demonstrated the effect of the viscosity ratio  $N$  on the fluid bearing effect. Three kinds of fluid systems including water-on-oil, oil-on-water, and water-on-air systems were used to cover the range of  $N$  from  $10^{-2}$  to  $10^1$ . For the water-on-oil flow, the continuous phases were the glycerol solutions with different concentrations while the enclosed fluid was paraffin oil, and the viscosity ratio  $N$  was  $O(10^{-2} - 1)$ . For the oil-on-water flow, the continuous phase was paraffin oil while the enclosed fluids were the glycerol solutions with different concentrations, and the viscosity ratio  $N$  was  $O(1 - 10)$ . For the water-on-air flow, water flowed over the cavities filled with air, so that the viscosity ratio  $N = 56$ . The percent change in drag reduction of the continuous phase,  $(Q_g - Q_0)/Q_0 \times 100$ , was plotted with the increasing viscosity ratios for the three fluid systems, as

shown in Fig. 4(d). The measured drag reduction effect increases as the viscosity ratio  $N$  increases, and the highest drag reduction of 23.5% is achieved on the water-on-air flow, which also agrees with the drag reduction result of the water flowing on a bubble mattress [19]. This result verifies that higher viscosity ratios result in larger drag reduction: the viscous fluid can be transported with less drag force by choosing fluids with lower viscosity as the fluid bearing. The fluid bearing effect has potential applications in microfluidics since the surface area to volume ratio increases as systems are scaled down.

#### IV. CONCLUSION

In summary, we fabricated microfluidic devices to flow viscous fluids over an immiscible fluid trapped in grooved channels. The fluid-fluid interface forms a no-slip/slip boundary for the continuous phase fluid flowing over it and vortices are formed in the grooves. Even for the modest protrusion of the fluid-fluid boundary into the main channel, the measured slip velocity at the fluid-fluid interfaces and the resultant effective slip length for the periodic no-slip/slip boundary agree with the theoretical predictions that assume a flat interface. Therefore, the vortices of the enclosed fluid act as a fluid bearing to lubricate the viscous flow in the microchannel, and the total drag reduction for water-on-oil, oil-on-water, and water-on-air fluid systems were measured for different viscosity ratios. This fluid bearing effect helps to overcome the increasing drag generated in the flow of high viscosity fluids in microchannels.

#### ACKNOWLEDGMENTS

This work was supported by the National Natural Science Foundation of China (Grants No. 51275266, No. 51322501, and No. 51275036). We thank Dr. C. Schönecher for helpful discussions, L. Liao for her help on the PIV images, and B. Dong for the support on the experiments.

#### APPENDIX A: GEOMETRICAL DIMENSIONS OF THE GROOVED MICROCHANNELS

Two different designs were utilized in the experiments, and the detailed dimensions of the designs are shown in Fig. 5. The design used in Figs. 1 and 2 is shown in Fig. 5(a), where the grooves are larger and close to each other, so that the design better illustrates the vortical structure of the flow field in the grooves. The design used in Figs. 3 and 4 is shown in Fig. 5(b), which gives better control on the shape of the fluid-fluid interfaces. Therefore, the shapes of the fluid-fluid interfaces at all the

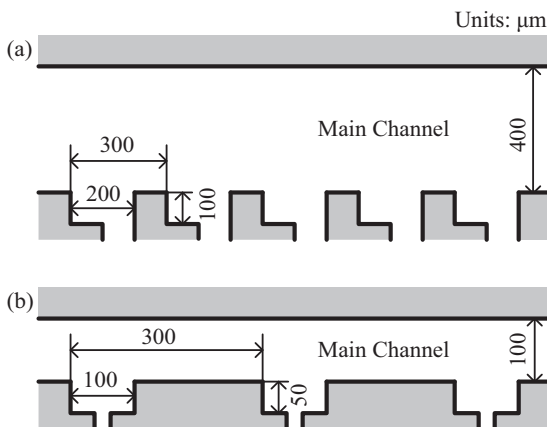


FIG. 5. The geometrical dimensions of the grooved microchannels used in the experiments. (a) The design used in Figs. 1 and 2. (b) The design used in Figs. 3 and 4. The height of all the channels is 25 μm.

grooves could be kept approximately flat during the experiments, so that we could neglect the effect of the shapes of the interfaces on the slip length and drag reduction.

### APPENDIX B: NORMALIZED SLIP VELOCITY AT THE FLUID-FLUID INTERFACE

As shown in Fig. 2(a), for  $|x| \leq b/2$  and  $y = 0$ , an effective slip boundary condition at the boundary is expressed [17] as  $u_c = N\gamma(x)\partial u_c/\partial y$ , where  $u_c$  is the  $x$  component of the velocity,  $\partial u_c/\partial y = \tau_c/\eta_c$ ,  $\tau_c$  is the shear stress,  $\gamma(x) = 2D[(b/2)^2 - x^2]^{1/2}$  is the local slip length distribution caused by the flow of the enclosed fluid in the grooves, and  $D = \gamma(0)/b$  is the normalized maximum slip length, so that  $u_c$  can be expressed as

$$u_c(x) = NDb \frac{\tau_c}{\eta_c} \sqrt{1 - \left(\frac{x}{b/2}\right)^2}. \quad (\text{B1})$$

For transverse flow over a rectangular cavity of depth  $h$ , width  $b$ , and infinite extension in the  $z$  direction, the normalized maximum slip length  $D$  is defined as

$$D = d_0 \operatorname{erf}\left(\frac{\sqrt{\pi}}{8d_0} A\right), \quad (\text{B2})$$

where the aspect ratio  $A = h/b$  and the constant  $d_0 = 0.124$  [17]. Consequently, in Eq. (B1),  $D$  is a constant for the same geometry used in the experiments. In addition, according to Ref. [17], the shear stress can be defined as  $\tau_c = \tau_\infty/(1 + 4DN)$ , where  $\tau_\infty$  is a given shear stress at infinity. Then, according to Eq. (B1),  $u_c$  can be further expressed as

$$u_c(x) = \frac{N}{1 + 4DN} \frac{\tau_\infty}{\eta_c} Db \sqrt{1 - \left(\frac{x}{b/2}\right)^2}, \quad (\text{B3})$$

where the value of  $\tau_\infty Db/\eta_c$  is a constant in different experiments with the same geometry and the same continuous phases. According to Eq. (B3),  $u_c(x)$  has an elliptic profile with a maximum velocity at  $x = 0$  as

$$u_c(0) = \frac{N}{1 + 4DN} \frac{\tau_\infty}{\eta_c} Db. \quad (\text{B4})$$

We use a normalized velocity when discussing the effect of the viscosity ratio  $N$  on the velocity distribution. We define a reference viscosity ratio  $N_{\text{ref}}$  and the corresponding velocity  $u_{\text{ref}}$  at the interface, and get the normalized velocity as

$$\frac{u_c(x)}{u_{\text{ref}}(0)} = \frac{N}{N_{\text{ref}}} \left(\frac{1 + 4DN}{1 + 4DN_{\text{ref}}}\right) \sqrt{1 - \left(\frac{x}{b/2}\right)^2}, \quad (\text{B5})$$

which leads to Eq. (1) in the main text.

For a rectangular cavity with the aspect ratio  $A = 1/2$ , Eq. (B2) gives  $D = 0.098$ . In our experiments, as the cavity is located on the side wall of the channel, the channel has a finite value of the dimensions in both  $y$  and  $z$  directions. Therefore, the fitted value of  $D = 0.027$  is correspondingly smaller than 0.098. Although the amplitude of the corresponding velocity is smaller than that in the flow configuration with infinite extension in the  $y$  and  $z$  directions, the velocity distribution at the fluid-fluid interface maintains a similar shape and similar variation with different viscosity ratios.

### APPENDIX C: EFFECTIVE SLIP LENGTH IN A RECTANGULAR MICROCHANNEL

In laminar flows, using the Navier slip boundary condition, the volume flow rate per unit length  $q$  of fluid in pressure-driven flow between two infinite parallel plates separated by a height  $H$  can

be expressed as [8]

$$q = \frac{H^3}{4\eta} \frac{\Delta p}{L} \left( \frac{1}{3} + \frac{\lambda_{\text{eff}}}{H} \right), \quad (\text{C1})$$

where  $\eta$  is the viscosity,  $\Delta p/L$  is the pressure gradient along the flow direction with the length of  $L$ , and  $\lambda_{\text{eff}}$  is the effective slip length. For laminar flow in a microchannel, which has a rectangular cross section with width  $W \gg$  height  $H$ , the volume flow rate can be expressed as [8,9]

$$Q = \frac{WH^3}{4\eta} \frac{\Delta p}{L} \left( \frac{1}{3} + \frac{\lambda_{\text{eff}}}{H} \right), \quad (\text{C2})$$

while the general form of the flow rate in a rectangular channel can be expressed as [9]

$$Q = \frac{WH^3}{c\eta} \frac{\Delta p}{L} \left( \frac{1}{3} + \frac{\lambda_{\text{eff}}}{H} \right), \quad (\text{C3})$$

where  $c$  is a constant, which is related to the geometry and can be obtained empirically. Therefore, the effective slip length  $\lambda_{\text{eff}}$  can be deduced from Eqs. (C2) and (C3) as

$$\lambda_{\text{eff}} = \left( \frac{Q}{Q_0} - 1 \right) \frac{H}{3}, \quad (\text{C4})$$

where  $Q_0$  is the volume flow rate in a microchannel with the same dimensions but without any slip, i.e.,  $\lambda_{\text{eff}} = 0$ .

- 
- [1] L. Bocquet and E. Lauga, A smooth future? *Nat. Mater.* **10**, 334 (2011).
- [2] H. Stone, A. Stroock, and A. Ajdari, Engineering flows in small devices: Microfluidics toward a laboratory-on-a-chip, *Annu. Rev. Fluid Mech.* **36**, 381 (2004).
- [3] G. Whitesides and A. Stroock, Flexible methods for microfluidics, *Phys. Today* **54**(6), 42 (2001).
- [4] J. P. Rothstein, Slip on Superhydrophobic Surfaces, *Annu. Rev. Fluid Mech.* **42**, 89 (2010).
- [5] P. Joseph, C. Cottin-Bizonne, J. M. Benoit, C. Ybert, C. Journet, P. Tabeling, and L. Bocquet, Slippage of Water Past Superhydrophobic Carbon Nanotube Forests in Microchannels, *Phys. Rev. Lett.* **97**, 156104 (2006).
- [6] C. Lee, C.-H. Choi, and C.-J. C. Kim, Structured Surfaces for a Giant Liquid Slip, *Phys. Rev. Lett.* **101**, 064501 (2008).
- [7] A. Tuteja, W. Choi, J. M. Mabry, G. H. McKinley, and R. E. Cohen, Robust omniphobic surfaces, *Proc. Natl. Acad. Sci. USA* **105**, 18200 (2008).
- [8] J. Ou, B. Perot, and J. Rothstein, Laminar drag reduction in microchannels using ultrahydrophobic surfaces, *Phys. Fluids* **16**, 4635 (2004).
- [9] Y. C. Jung and B. Bhushan, Biomimetic structures for fluid drag reduction in laminar and turbulent flows, *J. Phys.: Condens. Matter* **22**, 035104 (2010).
- [10] T.-S. Wong, S. H. Kang, S. K. Y. Tang, E. J. Smythe, B. D. Hatton, A. Grinthal, and J. Aizenberg, Bioinspired self-repairing slippery surfaces with pressure-stable omniphobicity, *Nature (London)* **477**, 443 (2011).
- [11] A. Lafuma and D. Quere, Slippery pre-suffused surfaces, *Europhys. Lett.* **96**, 56001 (2011).
- [12] D. Angelescu, T. Moscato, and R. V. Kujjk, Micro-structured surface having tailored wetting properties, US Patent No. US8859090 B2 (Oct. 14, 2014).
- [13] J. D. Smith, R. Dhiman, S. Anand, E. Reza-Garduno, R. E. Cohen, G. H. McKinley, and K. K. Varanasi, Droplet mobility on lubricant-impregnated surfaces, *Soft Matter* **9**, 1772 (2013).
- [14] B. R. Solomon, K. S. Khalil, and K. K. Varanasi, Drag reduction using lubricant-impregnated surfaces in viscous laminar flow, *Langmuir* **30**, 10970 (2014).

- [15] B. J. Rosenberg, T. Van Buren, M. K. Fu, and A. J. Smits, Turbulent drag reduction over air- and liquid-impregnated surfaces, *Phys. Fluids* **28**, 015103 (2016).
- [16] E. Lauga and H. Stone, Effective slip in pressure-driven Stokes flow, *J. Fluid Mech.* **489**, 55 (2003).
- [17] C. Schönecker and S. Hardt, Longitudinal and transverse flow over a cavity containing a second immiscible fluid, *J. Fluid Mech.* **717**, 376 (2013).
- [18] C. Schönecker, T. Baier, and S. Hardt, Influence of the enclosed fluid on the flow over a microstructured surface in the Cassie state, *J. Fluid Mech.* **740**, 168 (2014).
- [19] J. S. Wexler, I. Jacobi, and H. A. Stone, Shear-Driven Failure of Liquid-Infused Surfaces, *Phys. Rev. Lett.* **114**, 168301 (2015).
- [20] E. Karatay, A. S. Haase, C. W. Visser, C. Sun, D. Lohse, P. A. Tsai, and R. G. H. Lammertink, Control of slippage with tunable bubble mattresses, *Proc. Natl. Acad. Sci. USA* **110**, 8422 (2013).
- [21] F. Pan and A. Acrivos, Steady flows in rectangular cavities, *J. Fluid Mech.* **28**, 643 (1967).